PROCEEDINGS OF SPIE

Quantum Electronics Metrology

Alan E. Craig
Selim M. Shahriar
Editors

20–21 January 2008
San Jose, California, USA

Sponsored and Published by
SPIE

Volume 6906

Proceedings of SPIE, 0277-786X, v. 6906

The papers included in this volume were part of the technical conference cited on the cover and title page. Papers were selected and subject to review by the editors and conference program committee. Some conference presentations may not be available for publication. The papers published in these proceedings reflect the work and thoughts of the authors and are published herein as submitted. The publisher is not responsible for the validity of the information or for any outcomes resulting from reliance thereon.

Please use the following format to cite material from this book:
Author(s), "Title of Paper," in *Quantum Electronics Metrology*, edited by Alan E. Craig, Selim M. Shahriar, Proceedings of SPIE Vol. 6906 (SPIE, Bellingham, WA, 2008) Article CID Number.

ISSN 0277-786X
ISBN 9780819470812

Published by
SPIE
P.O. Box 10, Bellingham, Washington 98227-0010 USA
Telephone +1 360 676 3290 (Pacific Time) · Fax +1 360 647 1445
SPIE.org

Printed in the United States of America.

Publication of record for individual papers is online in the SPIE Digital Library.

SPIEDigitalLibrary.org

Paper Numbering: Proceedings of SPIE follow an e-First publication model, with papers published first online and then in print and on CD-ROM. Papers are published as they are submitted and meet publication criteria. A unique, consistent, permanent citation identifier (CID) number is assigned to each article at the time of the first publication. Utilization of CIDs allows articles to be fully citable as soon they are published online, and connects the same identifier to all online, print, and electronic versions of the publication. SPIE uses a six-digit CID article numbering system in which:

- The first four digits correspond to the SPIE volume number.
- The last two digits indicate publication order within the volume using a Base 36 numbering system employing both numerals and letters. These two-number sets start with 00, 01, 02, 03, 04, 05, 06, 07, 08, 09, 0A, 0B … 0Z, followed by 10-1Z, 20-2Z, etc.

The CID number appears on each page of the manuscript. The complete citation is used on the first page, and an abbreviated version on subsequent pages. Numbers in the index correspond to the last two digits of the six-digit CID number.

Contents

SINGLE PHOTONS

Conference Committee

Symposium Chair

Ali Adibi, Georgia Institute of Technology (USA)

Symposium Cochair

James G. Grote, Air Force Research Laboratory (USA)

Program Track Chair

Zameer U. Hasan, Temple University (USA)

Conference Chairs

Alan E. Craig, Montana State University, Bozeman (USA)
Selim M. Shahriar, Northwestern University (USA)

Program Committee

Hwang Lee, Louisiana State University (USA)
Lute Maleki, Jet Propulsion Laboratory (USA)

Session Chairs

1 Quantum Ensemble Metrology
Hwang Lee, Louisiana State University (USA)

2 Quantum Metrology Tools
Jonathan P. Dowling, Louisiana State University (USA)

3 Quantum Mechanics in Metrology
Selim M. Shahriar, Northwestern University (USA)

4 Clocks
Philip R. Hemmer, Texas A&M University (USA)

5 Interferometric Metrology
Hwang Lee, Louisiana State University (USA)

6 Single Photons
John C. Howell, University of Rochester (USA)

Introduction

This proceedings volume records the inaugural meeting of the conference on Quantum Electronics Metrology (QEM). New frontiers beckon as investigators explore the limits of precision in the physical world. Metrology is the apparent inheritor of such explorations, as instrumentation generally is among the early adopters of emerging technologies.

Broadly speaking, QEM encompasses two themes: quantum coherence and quantum entanglement. Quantum coherence has been at the forefront of precision metrology for a long time. Examples include atomic clocks, atomic magnetometer, atomic interferometer, SQUIDs, and so on. More recently, use of engineered dispersion, in the form of slow and fast light, for example, have led to prospects of revolutionary enhancements in precision interferometry, with applications to rotation sensing and gravitational wave detection. Another area of rapid progress is the use of trapped atoms and ions for optical clocks. Efforts are also underway to produce chip-scale atomic clocks by making use of novel advances in miniaturization of vapor cells.

Application of quantum entanglement to metrology is a more recent phenomenon. The use of squeezed light for enhanced precision in optical interferometry is the preeminent example. This idea continues to thrive, as mature and robust schemes are currently being pursued to improve the precision of gravitational wave detection using squeezed light. More recently, attempts are being made to enhance the precision of magnetometry, ranging, frequency measurement and imaging via the use of entangled states. The use of the so-called NOON states, employing multipartite entanglement, for precision interferometry as well as super-resolution lithography is a potentially promising development in this area.

In this conference, we have attempted to represent leading edge efforts in these two broad categories. More explicitly, the subscribed topics at this year's meeting comprised:

- interferometry incorporating ensemble and multipartite quantum entanglements
- interferometry incorporating quantum coherence
- delineation and characterization of quantum-optical phase;
- bridges between coherence and entanglement, often via the mechanism of quantum dispersion that produces slow and fast light
- single photon generation, propagation, and detection;
- chip-scale atomic clocks for robust usage and ultra-accurate clocks incorporating trapped ions and atoms

The eight papers in this volume will enable the readers to get a concise view of the latest development in these topics, both experimentally and theoretically. In addition, we have included, in the front matter, three other papers from the conference on Advances in Slow and Fast Light. These papers address important, complementary developments in the use of engineered dispersion for precision metrology.

QEM is an area of enormous interest for fundamental tests of the laws of nature, as well as for practical applications. We are confident that this field will continue to thrive, and this conference will grow in both size and impact in the coming years.

Alan E. Craig
Selim M. Shahriar

Quantum interference effects in rubidium vapor on a chip

Bin Wu[a], John Hulbert[b], Aaron R. Hawkins[b] , and Holger Schmidt[a]

[a]School of Engineering, University of CA Santa Cruz, 1156 High Street, Santa Cruz, CA 95064
[b]ECEn Department, Brigham Young University, 459 Clyde Building, Provo, UT 84602

ABSTRACT

Harnessing the unique optical quantum interference effects associated with electromagnetically induced transparency (EIT) on a chip promises new opportunities for linear and nonlinear optical devices. Here, we review the status of integrated atomic spectroscopy chips that could replace conventional rubidium spectroscopy cells. Both linear and nonlinear absorption spectroscopy with excellent performance are demonstrated on a chip using a self-contained Rb reservoir and exhibiting a footprint of only 1.5cm x 1cm. In addition, quantum interference effects including V-scheme and Λ-scheme EIT are observed in miniaturized rubidium glass cells whose fabrication is compatible with on-chip integration.

Keywords: Integrated optics, ARROW waveguides, quantum interference, nonlinear optics, EIT

1. INTRODUCTION

Recently, there has been a lot of activity in developing optical waveguides with hollow cores. This research is fueled by the wealth of applications that arise from being able to guide light through non-solid media such as liquids and gases with the convenience of integrated optics technology. Liquid-core waveguides are ideally suited for microfluidic and optofluidic applications in analytical chemistry, biology, and biomedicine. Continuing progress in this rapidly expanding field has enabled a variety of optical sensors, all the way to single molecule detection on a chip[1-3]. Equally big opportunities exist for gaseous media, molecular gases and atomic vapors, covering both miniaturization of well-established vapor spectroscopy techniques and the implementation of new functionalities by taking advantage of the waveguide confinement.

The major conventional areas of interest for vapor-filled optical waveguides are molecular detection/sensing in the atmosphere, precision spectroscopy[4], and frequency references and stabilization[5]. In addition, waveguides enable for the first time to harness optical quantum interference effects based on electromagnetically induced transparency (EIT)[6] in compact and practical structures. These effects include optical transparency[7], slow light[8], and nonlinear effects such as sum-frequency generation[9], parametric photon generation[10,11], cross-phase modulation[12], and quantum-nondemolition measurements using single photon detection[13]. The nonlinear effects benefit particularly from a waveguide environment as it allows for long optical interaction lengths (optical depths) with simultaneously small mode areas (high intensities). For example, it has been shown that dispersion-limited giant Kerr phase shifts can continue to increase down to waveguide cross sections of a few micrometers[12].

The most promising paths towards integrated atomic spectroscopy are based on using hollow-core photonic crystal fiber (HC-PCF)[14], antiresonant reflecting optical waveguides (ARROWs)[15], and nanophotonic slot waveguides[16]. HC-PCFs represent the most mature technology and allow for low loss propagation and large optical depths in the thousands. Saturated absorption spectroscopy in acetylene, EIT in acetylene, V-EIT and Λ-EIT in rubidium[17-21] have all been reported recently, and prove the feasibility of the integrated approach. Currently, the fiber gas cells are not completely self-contained as the fiber ends are typically placed within optically accessible vacuum cells connected to a pump apparatus. Completely miniaturized devices for atomic clock applications as well as saturated absorption spectroscopy have been developed at NIST where vapor cells with small volumes are constructed. However, these cells are not waveguiding structures, which limits the ratio of optical path length to beam area that is essential for nonlinear optics.

Advances in Slow and Fast Light, edited by Selim M. Shahriar, Philip R. Hemmer, John R. Lowell,
Proc. of SPIE Vol. 6904, 69040E, (2008) · 0277-786X/08/$18 · doi: 10.1117/12.773329

We are pursuing the integration of quantum interference effects in alkali vapors in monolithically integrated ARROW waveguides[22,23]. These allow for completely self-contained devices by adding the atomic reservoir to the chip, and providing the possibility to interface with other optical elements on the chip. Here, we review the status of these developments in the context of atomic spectroscopy with alkali vapors on a semiconductor chip.

2. ARROW WAVEGUIDES FOR ATOMIC SPECTROSCOPY

Fully self-contained integrated atomic spectroscopy devices have two principal characteristics: First, they enable light guiding through atomic vapors in hollow-core waveguides with micron-scale cross sections. Second, they provide an effective optical interface that couples the hollow waveguide section with solid-core wavegguides and seals the hollow section to eliminate the need for an external vacuum pump.

Figure 1a shows a side view of a hollow-core ARROW waveguide that fulfills these criteria. Built on a silicon substrate using a sacrificial core technique[24], waveguiding is ensured by surrounding the hollow core (index n_c) with high index layers whose thickness fulfills a well-known antiresonance condition[25]. While different dielectric materials can be used, the work presented here is based on alternating silicon nitride and silicon dioxide layers with thicknesses on the order of 100nm. Interfacing with solid-core waveguides on the chip is accmplished by aligning the topmost, thick SiO_2 layer with the hollow waveguide core so that light can be effectively coupled in and out of the vapor-containing space. To this end, the ARROW layers have to be transmissive at normal incidence as shown in Fig. 1a and reflective at grazing incidence at which the modes propagate inside the hollow core. This is indeed possible with our structures and illustrated by the photonic band diagram in Fig. 1b which shows propagation in a hollow core surrounded by a hypothetical infinite number of SiN and SiO_2 layers The white lines are the light lines for TE and TM modes, the horizontal dashed line represents the design wavelength, and the dashed and solid white arrows point to propagating modes being reflected at grazing incidence and being transmitted at normal incidence, respectively.

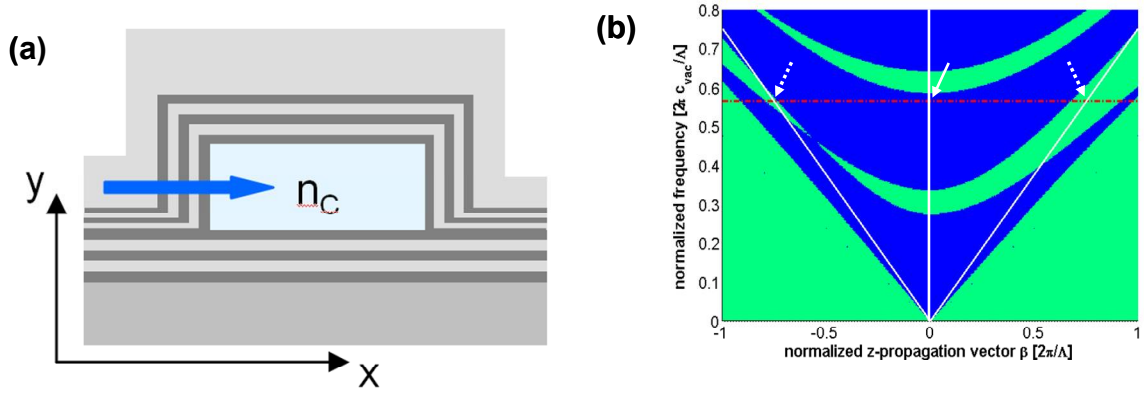

Fig. 1: a) Side view of hollow-core ARROW waveguide structure with core index n_c surrounded by dielectric layers (shades on grey) showing light enetring the hollow core from the top thick silcion nitride layer. b) representative photonic band structure for 1D photonic crystal composed of SiN and SiO_2 layers (blue area: forbidden band, green area: allowed band).

3. RUBIDIUM SPECTROSCOPY IN BULK CELLS

The key step for making integrated atomic vapor cells based on ARROW waveguides is the development of a suitable process to add a rubidium-containing reservoir on the chip. Several approaches have been developed. In a first approach, a stainless steel standoff was attached over one of the open ends of the hollow core with an epoxy adhesive. The other open end was sealed with a drop of epoxy. The chip was then placed in a controlled environment glovebox (Vacuum Atmospheres, Hawthorne, CA) filled with helium. Solid rubidium droplets were then transferred from a glass ampoule source into the stainless steel standoff. The top of the standoff was sealed using a stainless steel screw and butyl rubber o-ring, resulting in an integrated rubidium cell with helium buffer gas at atmospheric pressure. A more recent version of this process uses copper standoffs and sealing is accomplished by a combination of eoxy adhesive and crimping the top of the standoff with a commercial crimping tool, resulting in an improved seal.

x

In order to assess the performance of the seal, a set of test experiments with "minicells" (standard chromatography bottles) was carried out. A minicell sealed using the crimped copper approach is shown in the inset to Fig. 2b, showing shiny, metallic rubidium droplets at the bottom. The rubidium density in the cells was extracted from the hyperfine absorption spectra at the Rb D1 line. Fig. 2a shows how the atomic density evolves as it is subjected to repeated heating and cooling of the cell. It is seen that the density changes with temperature variation. However, the cell degrades with each heating cycle as is evident by the strongly reduced peak density of subsequent cycles. This observation is likely due to microscopic leaks that lead to slow oxidation of the Rb which limits the lifetime of the cell. Fig. 2b shows the same experiment with a different epoxy. Clearly, much higher peak densities along with significantly reduced degradation are observed. Fig. 2c shows a side-by-side comparison of the reduction in peak atomic density for the two different epoxies, again showing significant improvement. Minicells fabricated following this protocol can be heated repeatedly and are stable over several weeks. Most importantly, this fabrication method can be readily translated to integrated ARROW waveguides.

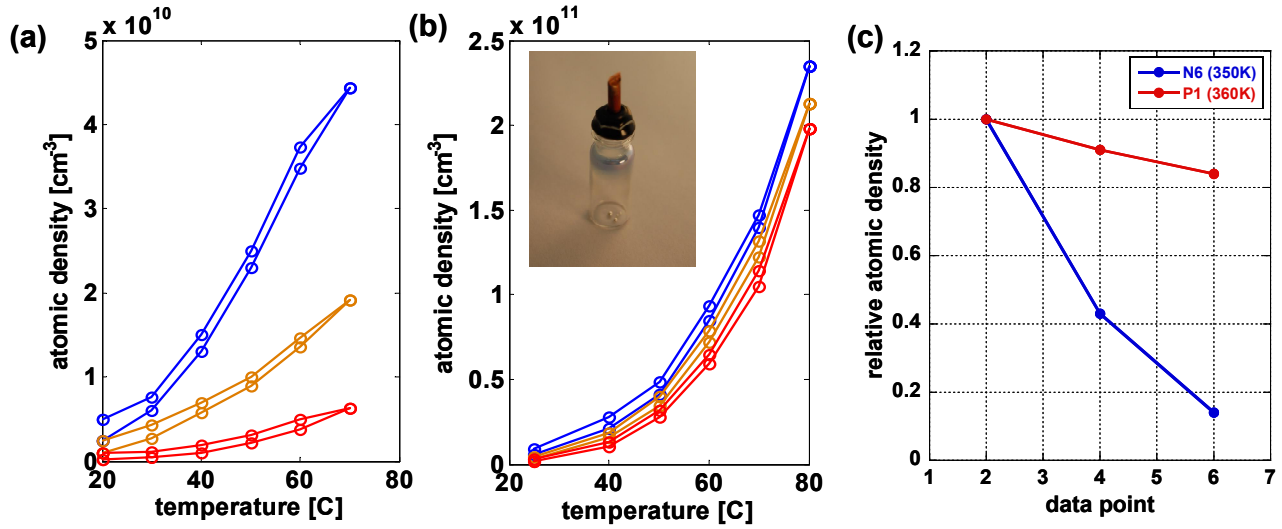

Fig. 2: Rb minicell performance a) atomic Rb vapor density in minicell with epoxy sealing subjected to repeated heating and colling cycles, b) same thermal cycling experiment with different epoxy, c) comparison of peak density over time for the two different epoxies.

4. LINEAR AND NONLINEAR RUBIDIUM SPECTROSCOPY ON A CHIP

Atomic spectroscopy on an integrated optical chip was demonstrated for the first time using cells fabricated with the original approach using stainless steel reservoirs and o-ring sealing. The hollow core dimensions of the waveguide were 5x12μm, and the solid core waveguide width was 12μm. The dielectric layer sequence for the ARROW waveguides was starting from the substrate (all values in nm): SiO_2/SiN/SiO_2/SiN/SiO_2/SiN – **core** – SiN/SiO_2/SiN/SiO_2/SiN/SiO_2 (550/110/550/110/550/110/**5000**/303/216/162/379/139/3402).

Fig. 3 shows the experimental layout for the different spectroscopic experiments. For linear spectroscopy, a probe beam from a tunable ECDL laser at the Rb D1 or D2 line was coupled into the solid-core waveguide using single-mode optical fiber.

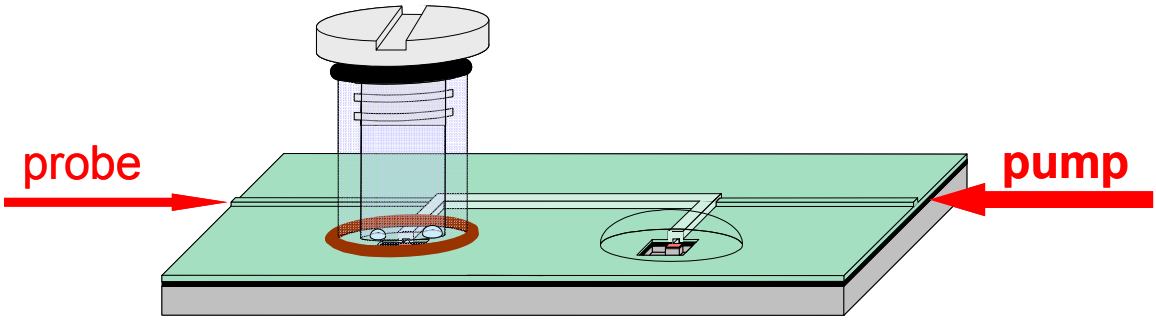

Fig. 3. Schematic layout of ARROW-based integrated rubidium cell on a chip.

Transmitted light was collected with an objective lens, focused on a photodetector, and recorded as a function of wavelength. Alternatively, the excitation beam could be directed to a conventional bulk rubidium reference cell. Fig. 4a shows the hyperfine structure of the Rb D2 line and the three transitions that could be probed with a single scan of the laser. Fig. 4b (top) shows the normalized hyperfine-split absorption spectra of the Rb D2-line around 780nm taken at a temperature of 70°C from an integrated ARROW rubidium cell. Clearly, the integrated Rb cell shows a clean, Doppler-broadened absorption signal that is nearly identical to that of the bulk cell, demonstrating the essential functionalities of the ARROW chip: confinement of both rubidium atoms and light within the same hollow-core waveguide. A key metric for the usefulness of an integrated rubidium cell, in addition to the ability to observe a guided mode and an absorption spectrum, are the levels of both atomic and optical density that can be achieved. In particular, it has been shown that EIT-based nonlinear effects require optical densities in excess of one to be practical[25]. We found that density levels in excess of two can be achieved in the integrated ARROW cell, corresponding to optically dense vapors. Higher optical densities can be achieved with longer hollow-core sections and by increasing the atomic density, e.g. using light induced desorption[21].

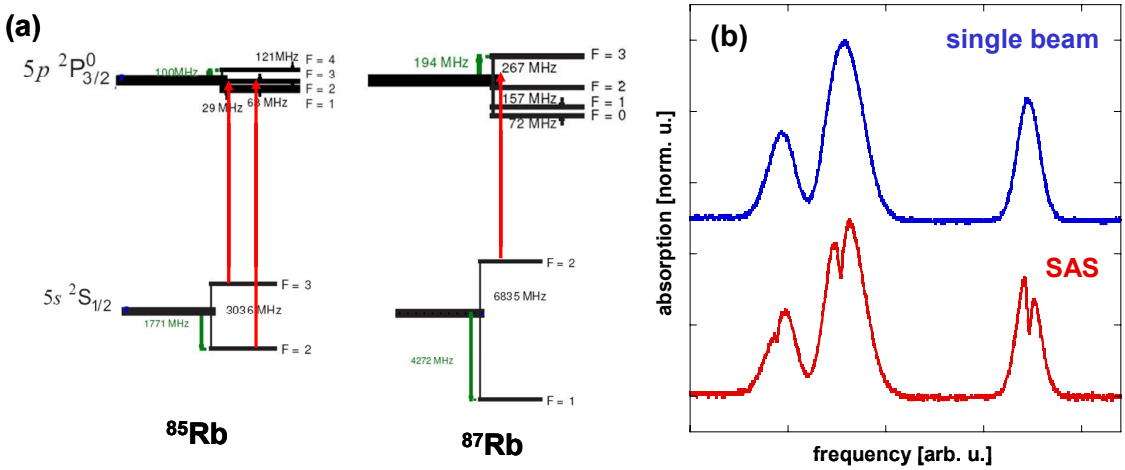

Fig. 4. a) Rb hyperfine structure and transitions probed during experiment, b) top: single beam absorption signal in integrated ARROW cell, bottom: saturated absorption spectroscopy in integrated ARROW cell using counterpropagating beams exhibiting characteristic lamb dips.

A second set of experiments was carried out to demonstrate one of the key advantages of our integrated approach and show a way towards near-term applications of this technology. The measurement setup was expanded to accommodate coupling light from both ends into the chip to demonstrate saturated absorption spectroscopy (SAS). SAS is a commonly used method for frequency stabilization of a light source by locking its emission frequency to that of an atomic transition. Typically, counterpropagating beams in bulk atomic vapor cells are used to create narrow spectral features by the elimination of Doppler broadening due to selection of atoms with zero velocity relative to the beams. The width of these Lamb dips is determined by the much smaller homogeneously broadened linewidth of the transition and leads to more accurate references. Normally, overlapping the strong pump with the weak probe beam requires some alignment

effort. In our integrated ARROW cell, however, this alignment is automatically accomplished by the optical waveguides, demonstrating one main advantage of the use of integrated optical elements. Fig. 4b (bottom) shows the SAS spectrum observed in the ARROW cell in the presence of the pump beam and clearly shows the characteristic Lamb dips.

Fig. 5 shows closeups of the three lamb dips (red dots) along with theoretical fits (blue lines) to a SAS lineshape that is given by[26]

$$\alpha(\nu,z) \sim 1 - \frac{S \cdot \gamma_S}{2\gamma\sqrt{1+S}} \frac{(\gamma/2)^2}{(\nu-\nu_0)^2 + (\gamma_S/2)^2} \qquad (1)$$

where S is a saturation parameter and γ is the homogeneous linewidth of the transition. Fig. 5 shows an excellent match of theory and experiment for S=2.2±0.1 and γ=46±5MHz. The lines are clearly not pressure broadened which indicates that the helium buffer gas has essentially escaped from the waveguide after fabrication was completed. The observed homogeneous linewidth is consistent with a predicted transit time broadening of 48MHz that is caused by the finite interaction time of a rubidium atom with a waveguide mode of a couple of microns width.

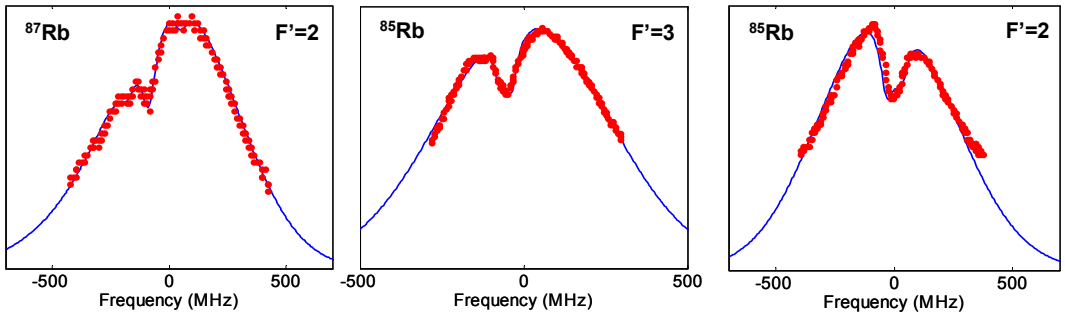

Fig. 5. Closeup of lamb dips from saturated absorption spectroscopy in ARROW cell. Red symbols: experiment, blue lines: fits to eqn. (1).

5. QUANTUM INTERFERENCE SPECTROSCOPY

Finally, we present the measurement of quantum interference effects in Rb-filled minicells described in section 3. First, electromagnetically induced transparency (EIT) was demonstrated in a V-configuration on the Rb D1 and D2 lines as illustrated in Fig. 6a. The V configuration has the advantage that the copropagating control and probe beams are easily separated based on their large wavelength difference.

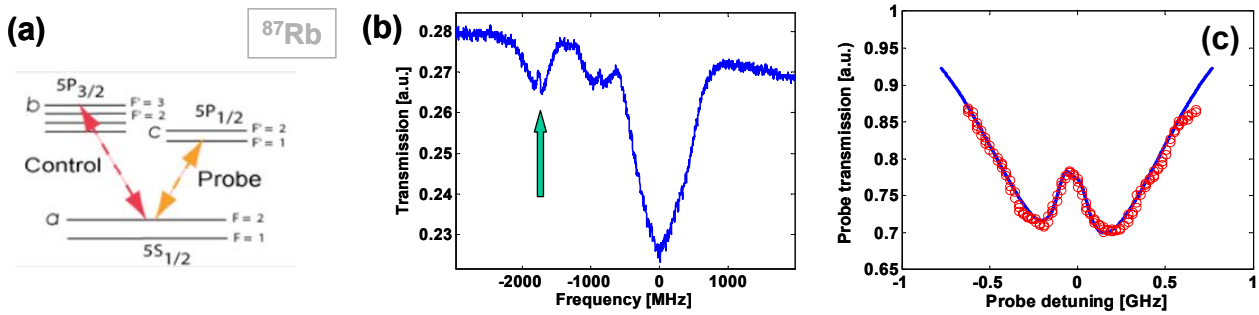

Fig. 6: V-scheme EIT in Rb minicell. a) atomic level configuration and applied laser fields, b) observed transmission spectrum, c) closeup of EIT peak along with fit to eqn. (2).

For the experiment, two spatially overlapping laser beams copropagated through approximately 1cm of Rb vapor inside a minicell. The resulting transmission spectrum of the D1 probe laser at 795nm is shown in Fig. 6b. An EIT transmission peak is clearly observed in the presence of the D2 coupling laser and marked by the arrow. Fig. 6c shows a closeup of the EIT peak along with a fit (blue line) to the equation for the linear susceptibility[27]

$$\chi = \frac{4i\hbar c\mu_{12}^2 N\sqrt{\pi}}{\varepsilon_0 u\omega_P} e^{z^2}\left[1 - erf(z)\right] \qquad (2)$$

Here, μ_{12} is the transition dipole moment, $\boldsymbol{N}$ is the atomic density, $\boldsymbol{u}$ is the atom velocity, ω_P is the probe frequency, ***erf*** is the error function, and $\boldsymbol{z}$ is given by

$$z = \frac{c}{u\omega_P}\left(\gamma_{21} - i\Delta_P + \frac{\Omega^2/4}{\gamma_{31} - i(\Delta_P - \Delta_C)}\right) \qquad (3)$$

Where γ_{21} and γ_{31} are the dephasing rates of the probe and control transitions, respectively, Ω is the control Rabi frequency, and Δ_P and Δ_C are the probe and control detunings, respectively. As can be seen in Fig. 6c, the agreement between experiment and theory is excellent, and allows us to extract a 2-1 dephasing rate of $\gamma_{21}/2\pi$=39MHz for the probe transition.

Secondly, Λ-EIT on the Rb D1 line was observed. Fig. 7a shows the generic three level scheme along with its implementation in ^{85}Rb. Generally, Λ-EIT can provide much narrower spectral features due to the long coherence time of the dipole-forbidden 2-1 transition. In addition, there are no contributions to the EIT transparency due to optical pumping as in the case of the V-scheme. For the experiment, two co-propagating and orthogonally polarized laser beams were aligned through a minicell. The control laser was tuned to the 2-3 resonance, and the probe laser was tuned across the 1-3 resonance.

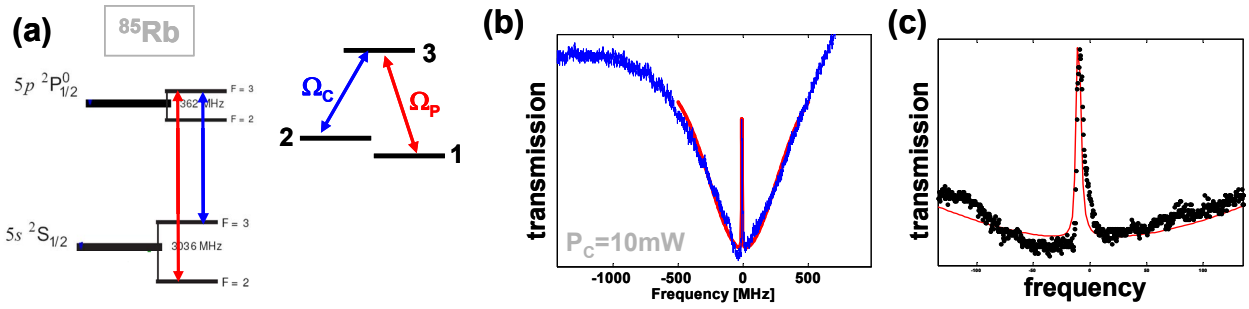

Fig. 7: a) Λ-EIT three level scheme and implementation in ^{85}Rb, b) probe transmission versus detuning from the 1-3 resonance, c) closeup of the EIT peak along with fit to theory (red line).

Fig. 7b shows the experimental result for the probe transmission (blue line) for a control beam power of P_c=10mW at room temperature. A clear transparency dip, the hallmark of quantum interference, is observed on resonance. The red line shows a fit to the theoretically expected absorption profile using an appropriately modified version of [??]. Again, very good agreement with the experimental data is found which is also illustrated in the closeup of the EIT peak region in Fig. 7c.

The control beam power was varied between 1mW and 10mW and both the depth and width of the EIT peak were extracted from the theory fits. These results are illustrated in Fig. 8. Fig. 8a shows the expected increase of the peak depth with the control laser Rabi frequency (intensity), showing that more than 65% transparency were easily achieved at room temperature. Fig. 8b shows the EIT linewidth which displays the expected linear dependence on the control Rabi frequency [??]. Finally, we extracted a coherence dephasing rate on the 2-1 transition of $\gamma_{21}/2\pi$=0.47 MHz which is much smaller than for the V-EIT scheme, as expected.

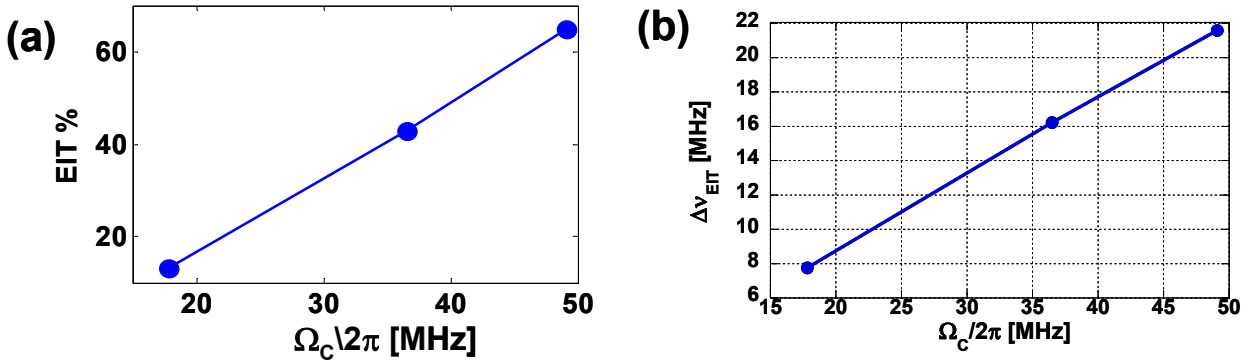

Fig. 8: relative depth (a) and width (b) of EIT peak versus control beam Rabi frequency.

6. CONCLUSIONS

Hollow-core waveguides continue to show progress towards novel linear and nonlinear optical devices when filled with atomic vapor. A new process for self-contained, monolithically integrated rubidium vapor cells using hollow-core ARROW waveguides was presented. Both linear and nonlinear atomic Rb spectroscopy on a chip was demonstrated along with high optical densities. The demonstration of various types of EIT in atomic vapor minicells fabricated with a waveguide compatible sealing process paves the way for realizing integrated quantum interference devices in the future.

ACKNOWLEDGMENTS

Support from the NSF and the DARPA/AFOSR Slow Light Program directed by J. Lowell under grants ECS-0500602 and FA-9550-05-1-0432 is gratefully acknowledged. We also acknowledge S. Harris and S. Du for providing the lasers for the Λ-EIT measurements.

REFERENCES

1. D. Yin, J.P. Barber, D.W. Deamer, A.R. Hawkins, and H. Schmidt, "Single-molecule detection sensitivity using planar integrated optics on a chip", Optics Letters **31**, 2136 (2006).
2. D. Yin, J.P. Barber, E. Lunt, D. Ermolenko, H. Noller, A.R. Hawkins, and H. Schmidt, "Planar single-molecule sensors based on hollow-core ARROW waveguides", Proceedings of the SPIE, vol. 6125, p. 61250Q (2006).
3. D. Yin, E.J. Lunt, A. Barman,A.R. Hawkins, and H. Schmidt, "Microphotonic control of single molecule fluorescence correlation spectroscopy using planar optofluidics" Optics Express 15, 7290 (2007).
4. Hänsch TW, Alnis J, Fendel P, Fischer M, Gohle C, Herrmann M, Holzwarth R, Kolachevsky N, Udem T, Zimmermann M. "Precision spectroscopy of hydrogen and femtosecond laser frequency combs", Phil. Trans. Royal Soc. London A **363**, 2155 (2005).
5. Danielli, A., Rusian, P., Arie, A., Chou, M. H. & Fejer, M. M., "Frequency stabilization of a frequency-doubled 1556-nm source to the $5S_{1/2}$ -$5D_{5/2}$ two-photon transitions of rubidium", Opt. Lett. 25, 905907 (2000).
6. Ghosh S, Sharping JE, Ouzonov DG, and Gaeta AL. "Coherent resonant interactions and slow light with molecules confined in photonic band-gap fibers", Phys. Rev. Lett. **94**, 093902 (2005).
7. A. Imamoglu and S.E. Harris, "Lasers without inversion: interference of dressed lifetime-broadened states", Opt. Lett., **14**, 1344, (1989).
8. L.V. Hau et al., "Light speed reduction to 17 metres per second in an ultracold atomic gas", Nature **397**, 594, (1999).

9. S.E. Harris and Y. Yamamoto, “Photon switching by quantum interference”, Phys. Rev. Lett., **81**, 3611, (1998).
10. D.A. Braje, V. Balic, G.Y. Yin, and S.E. Harris,”Low-light-level nonlinear optics with slow light”, Phys. Rev. A, **68**, 041801(R), (2003).
11. M.D. Lukin, P.R. Hemmer, M. Loffler, and M.O. Scully, “Resonant enhancement of parametric processes via radiative interference and induced coherence”, Phys. Rev. Lett., **81**, 2675, (1998).
12. H. Schmidt and A. Imamoglu, “Giant Kerr nonlinearities using electromagnetically induced transparency”, Opt. Lett., **21**, 1936, (1996).
13. A. Imamoglu, “High efficiency photon counting using stored light”, Phys. Rev. Lett., **89**, 3602 (2002).
14. Benabid F, Couny F, Knight JC, Birks TA & Russell PSJ. Compact, stable and efficient all-fibre gas cells using hollow-core photonic crystal fibers, Nature, **434**, 488 (2005).
15. D. Yin, J.P. Barber, A.R. Hawkins, and H. Schmidt, "Integrated ARROW waveguides with hollow cores", Optics Express, **12**, 2710, (2004).
16. Q. Xu, V. R. Almeida and M. Lipson, “Experimental demonstration of guiding and confining light in nanometer-size low-refractive-index material”, Optics Letters, **29**, 1626, (2004)
17. Ghosh S, Sharping JE, Ouzonov DG, and Gaeta AL. Coherent resonant interactions and slow light with molecules confined in photonic band-gap fibers, Phys. Rev. Lett. **94**, 093902 (2005).
18. R. Thapa et al., “Saturated absorption spectroscopy of acetylene gas inside large-core photonic bandgap fiber”, Opt. Lett., **31**, 2489 (2006).
19. Benabid F, Antonopoulos G, Knight JC, Russell PStJ. “Stokes amplification regimes in quasi-cw pumped hydrogen-filled hollow-core photonic crystal fiber”, Phys. Rev. Lett. **95**, 2139031 (2005).
20. Couny F, Light PS, Benabid F, Russell PStJ. “Electromagnetically induced transparency and saturable absorption in all-fiber devices based on C2H2-filled hollow-core photonic crystal fiber”, Opt. Comm., **263**, 28 (2006).
21. Ghosh S, Bhagwat AR, Renshaw CK, Goh S, Gaeta AL, Kirby BJ. “Low-light-level optical interactions with rubidium vapor in a photonic band-gap fiber”, Phys. Rev. Lett., **97**, 023603 (2006).
22. H. Schmidt, and A.R. Hawkins, "Electromagnetically induced transparency in alkali atoms integrated on a semiconductor chip", Appl. Phys. Lett., **86**, 032106 (2005).
23. H. Schmidt, D. Yin, W. Yang, B. Wu, D.B. Conkey, J.P. Barber, and A.R. Hawkins, "Towards integration of quantum interference in alkali atoms on a chip", Proceedings of the SPIE, **6130**, 613006 (2006).
24. J.P. Barber, D.B. Conkey, J. Lee, N.B. Hubbard, L. Howell, H. Schmidt, and A.R. Hawkins, "Fabrication of Hollow Waveguides with Sacrificial Aluminum Cores," IEEE Phot. Tech. Lett. **17**, 363, (2005)
25. M.A. Duguay, Y. Kokubun, T. Koch, and L. Pfeiffer, “Antiresonant reflecting optical waveguides in SiO2-Si multilayer structures”, Appl. Phys. Lett., **49**, 13, (1986).
26. Demtröder W. Laser Spectroscopy, 3rd ed., Springer2003.
27. Y. Li, M. Xiao, “Electromagnetically induced transparency in a three-level Λ-type system in rubidium atoms” Phys. Rev. A., **51**, 012703 (1995).
28. Ali Javan, Olga Kocharovskaya, Hwang Lee, and Marlan O. Scully, “Narrowing of electromagnetically induced transparency resonance in a Doppler-broadened medium”, Rev. A., **66**, 013805 (2002)

Simultaneous generation of slow and fast light for Raman coupled beams

G.S. Pati, M. Salit, K. Salit, S. Tseng and M.S. Shahriar
Department of EECS, Northwestern University, Evanston IL 60208

ABSTRACT

This paper presents an experiment to realize both slow and fast light effects simultaneously using the Raman gain and pump depletion in an atomic vapor. Heterodyne phase measurement shows the opposite dispersion characteristics at pump and probe frequencies. Optical pulse propagations in the vapor medium also confirm the slow and fast light effects due to these dispersions. The method being experimentally simple, and allowing the use of intense pulses experiencing anomalous dispersion via the fast light, can be applied in rotation sensing and broadband detection schemes proposed recently.

Key Words: slow light, fast light, Raman gain, rotation sensing, gravitational wave detection

1. INTRODUCTION

Resonant dispersion phenomena originating from optically induced coherence in atomic media have been used to produce both slow and fast light, and have the potential for many practical applications[1,2,3,4,5,6,7]. Subluminal (or slow) light propagation is observed when the dispersion profile has a positive slope (giving rise to a reduced group velocity), and has been shown in various types of material medium, including room temperature solids, using a variety of processes such as electromagnetically induced transparency[1,2], coherent population oscillation[8], and photorefractive beam coupling[9]. In contrast, controllable anomalous dispersion for superluminal (or fast) light propagation has only been demonstrated in the transparent intermediate spectral region corresponding to Raman gain doublets[4]. Recently, we proposed applications of this effect in ultra-sensitive rotation sensing[10] and also in designing a white light cavity for broadband gravity wave detection[11]. The Raman gain doublet method is not, however, appropriate for use with high power probe beams. An experimentally simpler method using depletion rather than double gain to create the anomalous dispersion would allow a high power beam to experience anomalous dispersion, a property which is useful in some of the applications mentioned above. Furthermore, the anomalous dispersion for the depleted pump is accompanied by a normal dispersion for the amplied probe, thus leading to simultaneous slow and fast light propagation in the same medium. For degenerate pump and probe with orthogonal polarizations, this also opens up the possibility of studying polarization rotation accompanied by pulse cleaving and re-merger.

Raman gain is observed in a three-level atomic medium under the two-photon resonance condition, as illustrated by the energy level diagram in figure 1. It is normally achieved by applying a strong coupling laser that creates both population inversion and drives a stimulated Raman process[12]. Under this condition, the atomic medium behaves as a two-photon gain medium. Single-pass Raman gain with a large gain coefficient and subnatural linewidth can be achieved using a medium with modest atomic density [$N \sim O(10^{12})$] and ground-state dephasing. Experimentally, self-pumped off-resonant Raman gain can be observed using frequency-detuned pump lasers detuned far below the atomic resonance. However, gain can also be extracted more efficiently using a relatively weak pump laser intensity and observed over a wide range of frequency detunings, if optical pumping is used to create the population inversion between the two coherently coupled ground states. During the stimulated two-photon Raman transition, the pump energy gets depleted as the pump photons are converted to produce the probe photons. This creates a situation where the probe frequency experiences a positive dispersion (subluminal effect), while the pump frequency experiences a negative dispersion (superluminal effect). We have investigated this experimentally and observed both these effects simultaneously in the atomic vapor medium.

Advances in Slow and Fast Light, edited by Selim M. Shahriar, Philip R. Hemmer, John R. Lowell,
Proc. of SPIE Vol. 6904, 69040L, (2008) · 0277-786X/08/$18 · doi: 10.1117/12.772236

2. EXPERIMENTAL DETAILS

Our experiment uses a spatially non-overlapping incoherent optical pump and a moderate Raman pump intensity. For observing gain, an off-resonant Raman excitation is constituted in a Λ-type configuration using the hyperfine ground states and the Doppler-broadened unresolved hyperfine $5P_{3/2}$ excited state manifolds of the D2 line in Rb^{85}. Fig. 2 shows the schematic of our experimental setup. The probe and pump laser beams are obtained using separate accousto-optic modulators (AOMs) from an external cavity frequency-locked CW Ti:Sapphire laser (line width ~ 1 MHz). The frequency difference between them is matched to the ground state splitting in Rb^{85} (3.0357 GHz) for two-photon resonance. An incoherent beam from a tapered amplifier diode laser is used as an optical pump to populate the lower ground state. Raman gain at the probe frequency is observed by scanning the probe around the two-photon resonance. The pump and probe beams are linearly and orthogonally polarized for the stimulated Raman process. A 10 cm long rubidium vapor cell containing mixtures of both the 85 and 87 isotopes is used in the experiment. The vapor cell is magnetically shielded using two-layers of μ-metal. During the experiment, the cell is also heated to nearly a steady temperature of 70°C using bifilarly wound coils that produce a negligible axial magnetic field. All the beams are combined using a polarizing as well as non-polarizing beam splitters at the input end before being sent through the cell. After passing through the vapor cell, the probe beam is separated from all the other beams by using a high extinction prism polarizer (the spatially non-overlapping optical pump beam does not fall on the detector and therefore does not have to be separated out). Rubidium atoms moving with an average thermal velocity (~ 300 m/sec), diffuse through the cross-section of the non-overlapping optical pump beam and get optically pumped. A strong optical pump beam (~ 20 mW) has been used to ensure optical pumping over large velocity group of atoms required for population inversion and gain.

Stimulated Raman gain is considered as a two-step process where a relatively intense incoherent pump field acts on the upper ground state F=3 creates population inversion between the two ground states, and the pump and probe then excite a Raman transition to produce gain at the probe frequency. While observing the probe gain, we vary the average frequency detuning of the laser fields for the Raman transition by tuning the laser frequency away from the $5S_{1/2}$, F = 3 - $5P_{3/2}$ F′ = 4 transition. Maximum probe gain is observed for a detuning close to 1 GHz below the transition. When this happens, the pump energy is depleted due to the energy transfer from pump to probe. Thus the two-photon resonance can also be observed in pump depletion. Figure 3a shows the gain in the probe and corresponding depletion of the pump beam.

We then used a heterodyne technique to accurately measure the dispersion associated with probe gain and pump depletion (figure 3b). A non-resonant auxiliary beam is produced by frequency shifting (by 80 MHz) a fraction of the probe beam using an acousto-optic modulator. This is then divided in two parts, one of which is combined with the probe that experiences Raman gain and the other with the unperturbed fraction of the probe that does not propagate through the cell. These two heterodyne signals are detected using two fast photodetectors. The phase difference between the two rf signals varies in response to probe dispersion as the probe frequency is scanned around the gain resonance. A low phase noise mixer and a low-pass frequency filter are used to demodulate the rf signal from the detectors. The amplitude of the demodulated signal is proportional to the refractive index variation in the dilute atomic medium. A similar heterodyne technique was used to measure the dispersion due to pump depletion in fig. 3b by using an auxiliary frequency shifted pump beam shown in dashed line in fig. 2. This beam is blocked during the probe dispersion measurement, but turned on during the pump dispersion measurement. The polarizer and the half-wave plate in the unperturbed and perturbed beam paths are also rotated to measure the pump dispersion using the same experimental arrangement. The sign of dispersion is observed to be opposite and negative in comparison with the probe.

Having determined in this way that the theoretical group velocity a pulse centered at the probe frequency should be less than c_0, due to the positive slope of the dispersion profile at its frequency, and that the group velocity for a pulse at the pump frequency should be greater than c_0 due to the negative slope of the dispersion at that frequency, we next used optical pulses in these beams so that their group velocities could be measured directly.

The beams were pulsed using an RF switch on the voltage controlled oscillator (VCO) which generates the drive frequency for the AOM. Turning the switch off and on with TTL pulses from a digital pulse generator turns the AOM on and off quickly, creating, effectively, square pulses at the pump and probe. Square pulses, however, are not

suitable for these group velocity measurements since they have many frequency components outside the dispersion bandwidth. The VCO output was therefore passed through a mixer and multiplied with a low-pass filtered TTL pulse before being amplified and connected to the AOM transducer. The pulses created had smooth rise and falling edges, but had the two lobed shape which is evident in figure 4 and figure 5 (the shapes of these lobes also differ because of two different frequency mixers that were used for the two beams) Figure 4 shows the delay and gain experienced by the probe pulse in the presence of the pump. The transmission of the probe in the absence of the pump is shown by the black line, and the transmission when the pump beam is on, by the red line. The peak of the pulse clearly emerges later in the presence of gain, and the re-shaped pulse takes longer to fully emerge from the medium, as shown by the long "tail" on the red line. For reference, we also recorded a pulse which was routed around the material and experienced no dispersion, shown in blue. The smaller amplitude is due to the imperfect beam splitter used to separate this pulse from the pulse which was sent through the medium.

Figure 5 shows similar data for the pump pulse, but in this case the dashed line represents propagation of the pump pulse in the absence of the probe beam, and the solid line represents the propagation of the pump when the probe beam is on. Here the difference is less dramatic, but still clear. The solid line shows the reduction in amplitude due to the depletion of the pump beam, and a very slight advancement at the leading edge, and a more significant one at the trailing edge. The group velocity of this pulse is greater than c_0, due to the anamolous dispersion it experiences.

3. CONCLUSION

This data confirms that the same medium may simultaneously act as a slow light medium for pulses centered at one frequency and a fast light medium for pulses centered at a different frequency. It also points to a simple method of creating steep anomalous dispersion profiles for high power beams, which promises to be useful in the applications we are pursuing for rotation sensing and gravitational wave detection. This work was supported in part by the Hewlett-Packard Co. through DARPA and the Air Force Office of Scientific Research under AFOSR contract no. FA9550-05-C-0017, and by AFOSR Grant Number FA9550-04-1-0189.

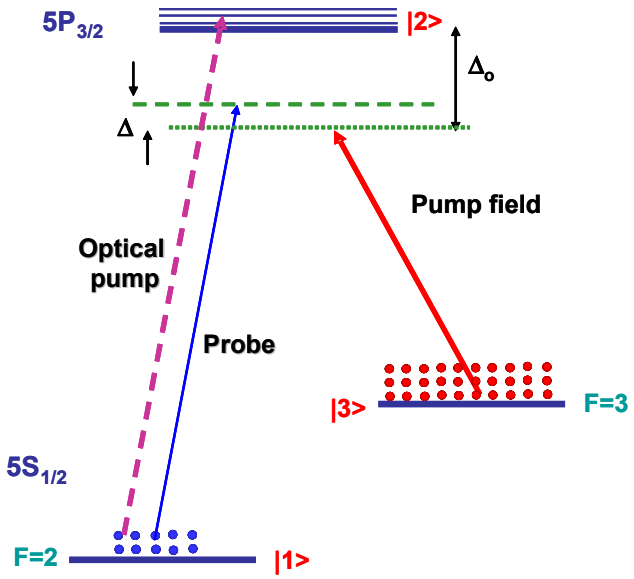

Figure 1. Energy level structure in D_2 line of ^{85}Rb used in Raman gain and depletion experiment

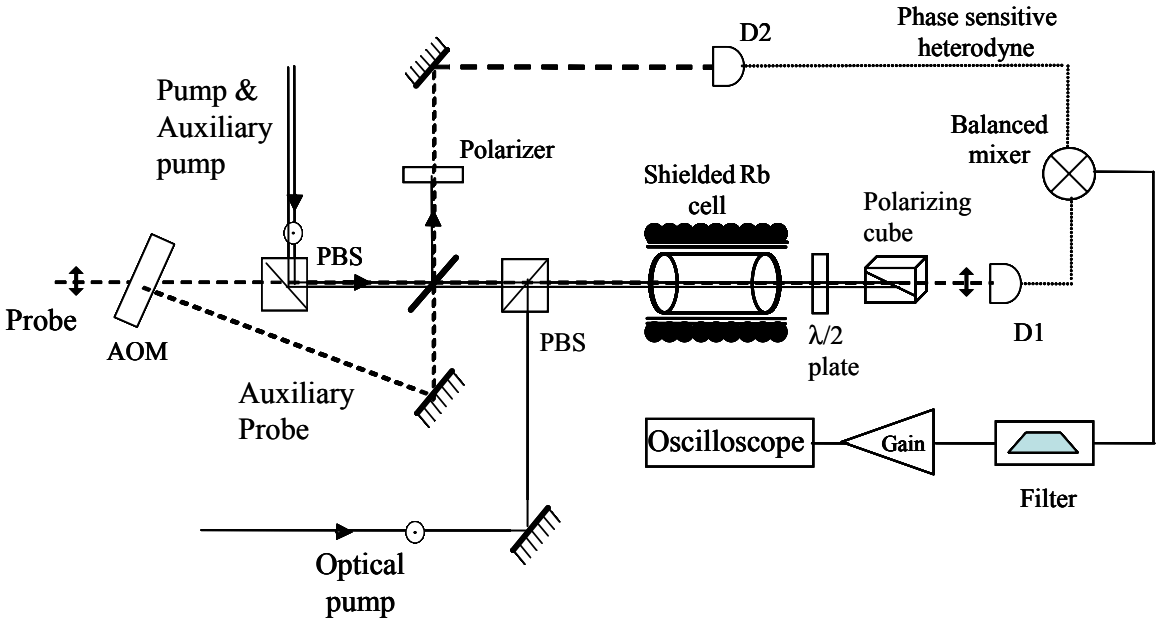

Figure 2. Experimental arrangement. PBS, polarizing beam splitter, AOM, acousto-optic modulator, D, photodiode

xx

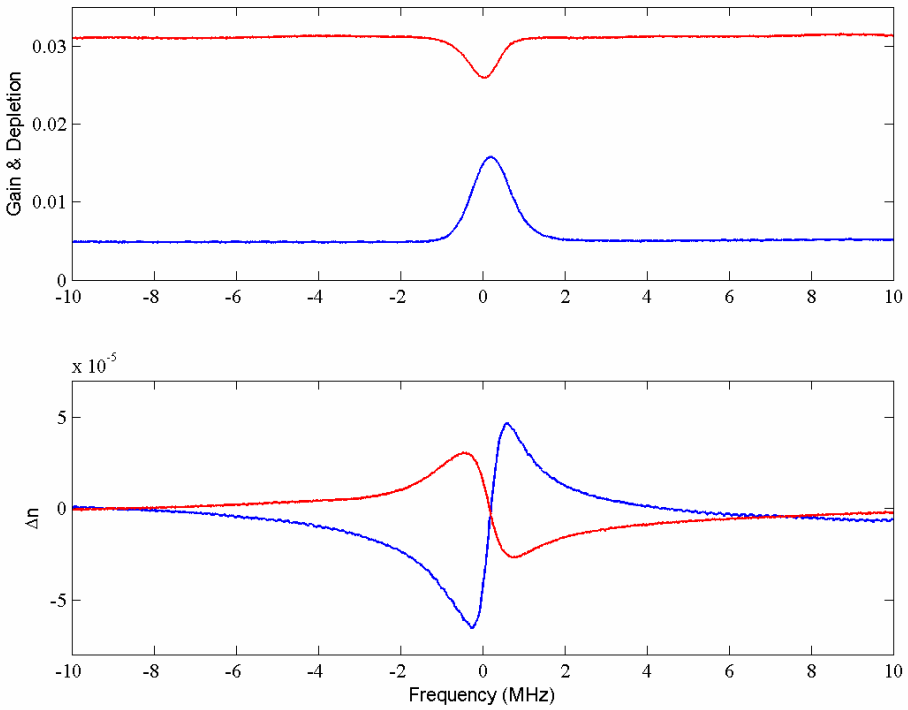

Figure 3. (a) measured gain and depletion, (b) corresponding dispersions measured using the heterodyne technique.

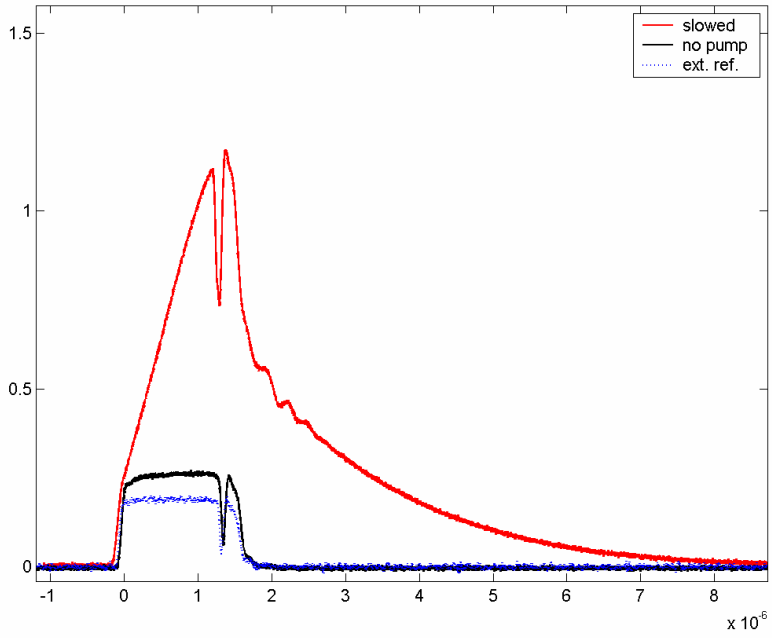

Figure 4. Probe pulse slowing using gain induced positive dispersion

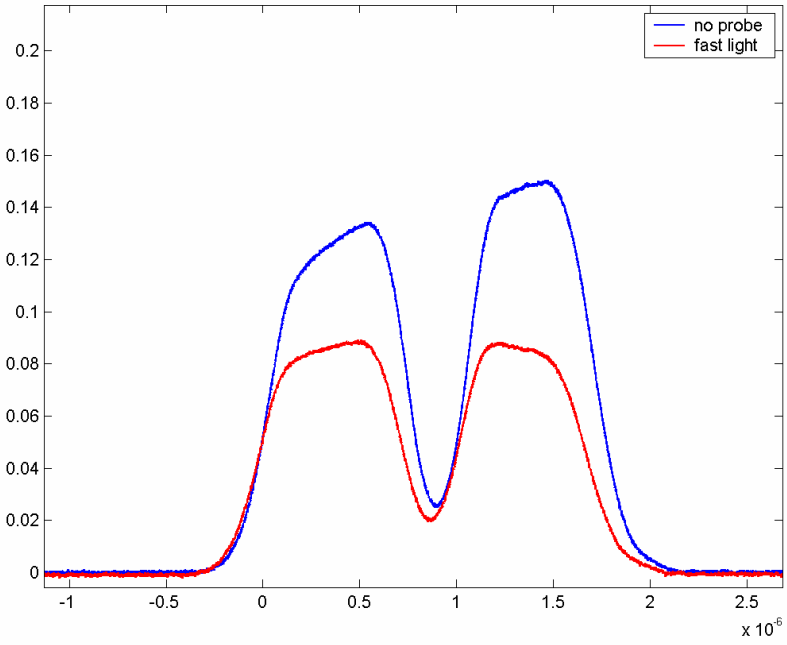

Figure 5. Pump pulse advancement (fast light) using depletion induced negative dispersion

REFERENCES

[1] M. M. Kash, V. A. Sautenkov, A. S. Zibrov, L. Hollberg, G. R. Welch, M. D. Lukin, Y. Rostovtsev, E. S. Fry and M. O. Scully, "Ultraslow Group Velocity and Enhanced Nonlinear Optical Effects in a Coherently Driven Hot Atomic Gas", Phys. Rev. Lett. 82, 5229 (1999).

[2] A.V. Turukhin, V.S. Sudarshanam, M.S. Shahriar, J.A. Musser and P.R. Hemmer, "Observation of Ultraslow and Stored Light Pulses in a Solid", Phy. Rev. Lett., 88, 023602 (2002).

[3] A. M. Steinberg and R. Y. Chiao, "Dispersionless, highly superluminal propagation in a medium with a gain doublet", Phys. Rev. A 49, 2071 (1994).

[4] A. Dogariu, A. Kuzmich, and L. J. Wang "Transparent anomalous dispersion and superluminal light-pulse propagation at a negative group velocity", Phys. Rev. A 63, 053806 (2001).

[5] A. B. Matsko, D. V. Strekalov and L. Maleki, "On the dynamic range of optical delay lines based on coherent atomic media", Opt. Exp. 13, 2210 (2005).

[6] D.F. Phillips, A. Fleischhauer, A. Mair, R.L. Walsworth and M.D. Lukin, "Storage of Light in Atomic Vapor", Phys. Rev. Lett. 86, 783 (2001).

[7] S.E. Harris and Y. Yamamoto, "Photon Switching by Quantum Interference", Phys. Rev. Lett. 81, 3611(1998).

[8] M. S. Bigelow, N. N. Lepeshkin,and R. W. Boyd, "Observation of Ultraslow Light Propagation in a Ruby Crystal at Room Temperature" , Physical Review Letters, Vol. 90, 113903 (2003) .

[9] A. Shumelyuk, K. Shcherbin, S. Odoulov, B. Sturman, E. Podivilov, and K. Buse, "Slowing Down of Light in Photorefractive Crystals with Beam Intensity Coupling Reduced to Zero", Phys. Rev. Lett. 93, 243604 (2004).

[10] M.S. Shahriar, G.S. Pati, R. Tripathi, V. Gopal and M. Messall , "Ultrahigh enhancement in absolute and relative rotation sensing using fast and slow light", Phys. Rev. A, 75, 053807 (2007).

[11] G.S. Pati, M. Salit, K. Salit, and M.S. Shahriar, "Demonstration of a Tunable-Bandwidth White Light Interferometer using Anomalous Dispersion in Atomic Vapor", Phys. Rev. Lett. 99, 133601,(2007).
[12] P. Kumar and J.H. Shapiro, "Sodium Raman laser: direct measurements of the narrow-band gain", Opt. Lett. 10, 226 (1985).

Active Slow-Light Rotation Sensor

Jacob Scheuer* and Ben Z. Steinberg
School of Electrical Engineering, Tel-Aviv University, Ramat-Aviv, Israel 69978

ABSTRACT

We study the lasing eigen-modes and dynamics of circular coupled laser array in a rotating framework for ultra-sensitive integrated optical rotation sensing applications. The dependence of the mode and frequency splitting on the array parameters is studied in details. The impact of variations of the resonance wavelength of the individual cavities and the inter-cavity coupling is studied and found to generate a "dead-zone" which limits the sensitivity of the sensor.

Keywords: Gyroscopes, Sagnac Effect, Integrated optics devices

1. INTRODUCTION

An electromagnetic wave propagating along a circular path in a rotating medium accumulates additional phase shift which depends on the medium rotation. This phase shift, known as the Sagnac effect, is the underlying mechanism of contemporary high-resolution optical rotation sensors and Gyros. Optical rotation sensors can be roughly divided into two sub-categories: 1) Passive devices that generally measure the phase shift between the clockwise (CW) and counterclockwise (CCW) rotating waves using interferometric methods and 2) Active devices (lasers) that measure the beating between the resonance frequencies of the CW and CCW rotating waves[1]. The detection threshold of Gyros belonging to these sub-categories is limited by different mechanisms. Passive devices are basically limited by the minimal power which can be detected, which is determined by Schott noise while laser Gyros are theoretically limited by a phenomenon called injection locking which tends to lock the frequencies of the CW and CCW rotating waves at low rotation rates. This frequency locking is caused by undesired reflections and backwards scattering of one mode to the other due to imperfections in the optical path. However, the injection locking phenomenon can be eliminated by employing various techniques[1] such as biasing the Gyro using a known rotation rate, etc. As a result, laser Gyros are more commonly used then their passive counterpart, especially when the detection of very low rotation rates are desired. Nevertheless, the *responsivity*, which determines the device accuracy, of both active and passive devices is determined almost solely by the area circumvented by the optical path[2], thus necessitating relatively large devices.

Recently, the Sagnac effect was studied in slow-wave structures consisting of single and multi mode coupled micro-cavities[3, 4]. These studies demonstrated the slow-wave structure potential for responsivity enhancement while retaining compact dimensions. In particular, it was found that the Sagnac effect is manifested differently in slow-wave structure and that the responsivity is determined not only by the area of the device. Other parameters such as number of cavities, inter-cavity coupling and the area of the individual cavities play a role in determining the Gyro responsivity[3-5].

These studies, however, where focused on *passive* devices which exploit the difference in the phase accumulated by the CW and CCW rotating waves. Generally speaking, the performances of passive CROW based devices, particularly CROW delay lines, are inherently limited by the losses (i.e. the Q-factor) of the individual cavities[6]. Recently, it was suggested to incorporate gain into the cavity to overcome this problem[7]. Here we study *active* slow-wave rotation sensors in which each cavity is a micro-laser. A realization of such structure employing a circular array of vertical cavity surface emitting lasers (VCSELs) is depicted in Fig. 1. Unlike continuous optical path ring lasers (such as fiber lasers) the "backwards scattering" in a coupled resonator optical waveguide (CROW) structure is inherently manifested by the inter-laser coupling coefficient and does not need to be introduced phenomenologically.

In Sec. 2 we present the theoretical framework and derive a set of rate equations for the circular laser array. In Sec. 3 we study the lasing modes and dynamics of the array. In Sec. 4 we study the effect of structural variations and inaccuracy on the device performance. In Sec. 5 we discuss the results and summarize.

*kobys@eng.tau.ac.il; Phone: +972-3-6407559; Fax: +972-3-6423508; www.eng.tau.ac.il/~kobys/

Advances in Slow and Fast Light, edited by Selim M. Shahriar, Philip R. Hemmer, John R. Lowell,
Proc. of SPIE Vol. 6904, 69040O, (2008) · 0277-786X/08/$18 · doi: 10.1117/12.772231

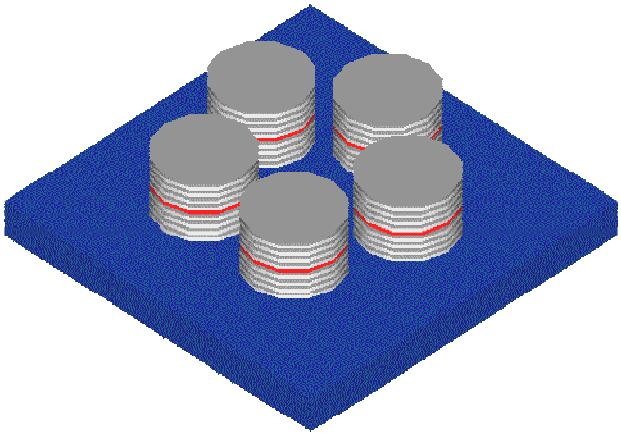

Fig. 1. Active CROW gyro based on a circular array of VCSELs

2. THEORETICAL FRAMEWORK

2.1 The passive CROW

We base our derivation of the passive CROW based gyroscope on the tight-binding approach adopted to rotating system[3], in conjunction with the array rate equations on the notations and definitions of Ref. 8. We assume that each single microcavity with center at $\vec{r}_n$ has a (complex) dielectric profile $\varepsilon_C(\vec{r}-\vec{r}_n)$ supporting a single mode with resonance frequency ω_0 and field profile $\psi(\vec{r}-\vec{r}_n)$ at stationary conditions:

$$\nabla^2\psi = -\varepsilon_C\left(\vec{r}\right)\frac{\omega_0^2}{c^2}\psi \tag{1}$$

The wave equation describing the total field in a *rotating* laser array is given by:

$$\nabla^2 E = -\varepsilon\left(\vec{r}\right)\frac{\omega^2}{c^2}E + 2i\frac{\omega^2}{c^2}\frac{\Omega}{\omega}\frac{\partial}{\partial\theta}E \tag{2}$$

where $\varepsilon(\vec{r})$ is the dielectric coefficient of the whole structure, c is the speed of light, ω - the optical frequency of the field, Ω - the (mechanical) rotation frequency and $E\left(\vec{r}\right)$ is the electrical field profile. It should be noted that both ε and ε_C have real an imaginary parts, i.e. $\varepsilon_C(\vec{r}) = \varepsilon_C^R(\vec{r}) + i\varepsilon_C^I(\vec{r})$, $\varepsilon(\vec{r}) = \varepsilon^R(\vec{r}) + i\varepsilon^I(\vec{r})$. Therefore, we normalize the mode profile of the individual laser according to $\int \varepsilon_C^R(r)\psi(r)\psi^*(r)d^3r = 1$. To solve Eq. (2), we adopt the extended tight binding approach and expand the total field of the rotating system using the modes of the isolated and stationary micro-cavities:

$$E = \sum_{n=1}^{L} A_n\psi(\vec{r}-\vec{r}_n) \tag{3}$$

where L in the number of lasers, and $\vec{r}_n$ is the center of the n cavity. Due to the tight-binding (weak coupling) assumption, the effect of inter cavity coupling, as well as the effect of rotation, are manifested essentially via the (yet unknown) expansion coefficients A_n. Note that the relevant wave equation for the total field (2) is no longer self adjoint (due to rotation), thus the variational solution procedure usually employed in tight-binding theory cannot be invoked. Instead, we follow the steps: introducing (3) and (1) into (2), multiplying both sides by $\psi^*\left(\vec{r}-\vec{r}_m\right)$, and keeping only the exponentially dominant terms (nearest neighbor coupling). The result is the matrix equation for the field expansion coefficients A_m (m=1..L):

$$\Delta\omega A_m\left(1+i\delta\right) = \tfrac{1}{2}\omega_0\left|\kappa_1\right|e^{i\varphi_\kappa}\left(A_{m-1}+A_{m+1}\right) - \tfrac{1}{2}\omega_0 A_m\left|\Delta\alpha\right|e^{i\varphi_{\Delta\alpha}} + i\omega_0\Omega\gamma_1\left(A_{m+1}-A_{m-1}\right) \tag{4}$$

where we assume $\omega \approx \omega_0$, define $\Delta\omega = \omega - \omega_0$ and

$$\begin{aligned}
\kappa_1 &= \int \left[\varepsilon_C \left(\vec{r} - \vec{r}_2 \right) - \varepsilon \left(\vec{r} \right) \right] \psi \left(\vec{r} - \vec{r}_2 \right) \psi^* \left(\vec{r} - \vec{r}_1 \right) d^3 r \\
\Delta\alpha &= \int \left[\varepsilon \left(\vec{r} \right) - \varepsilon_C \left(\vec{r} - \vec{r}_m \right) \right] \left| \psi \left(\vec{r} - \vec{r}_m \right) \right|^2 d^3 r \\
\delta &= \int \varepsilon_C^I \left(\vec{r} \right) \left| \psi \left(\vec{r} \right) \right|^2 d^3 r \\
\gamma_1 &= \int \frac{\partial}{\partial \theta} \psi \left(\vec{r} - \vec{r}_2 \right) \psi^* \left(\vec{r} - \vec{r}_1 \right) d^3 r
\end{aligned} \tag{5}$$

We assume that the imaginary part of the refractive index is relatively small, i.e. $\delta << 1$ and, therefore, the coefficient multiplying A_m on the LHS of (4) merely introduces a negligible phase shift. The assumption is valid because in all practical devices (lasers) $\varepsilon^I << \varepsilon^R$. $\Delta\alpha$ is also, in principle, complex but its impact can be divided into a frequency shift (the real part) and gain shift (imaginary part) for each individual laser and, thus, can be absorbed into the resonance frequency and cavity loss of each laser. The significant contribution stemming for the imaginary part of the refractive index is expressed in ϕ_κ (nearest neighbor coupling). This phase is strongly affected by the guiding mechanism of the mode of lasers (gain or index). For example, in the case of pure gain guided lasers κ_1 is purely imaginary ($\phi_\kappa = \pi/2$) Therefore, this phase cannot be neglected.

2.2 The active CROW rate equations

To derive the rate equations for temporal evolution of the slowly varying field envelope of E we assume the following: The time dependent amplitude of the field in each cavity can be represented by a Fourier integral - $A_m(t) = \int \hat{A}_m(\omega) \exp(i\omega t) d\omega$. This amplitude is assumed to have a relatively narrow bandwidth around ω_0, i.e. $A_m(t) = E_m(t) \exp(i\omega_0 t)$ and therefore $E_m(t) = \int \hat{E}_m(\Delta\omega) \exp(i\Delta\omega t) d\Delta\omega$ where $\Delta\omega = \omega - \omega_0$. By inverse Fourier transforming equation (4) we get a set of coupled ordinary differential equations describing the temporal evolution of the field in each micro-laser:

$$\frac{dE_m}{dt} = \tfrac{1}{2} i\omega_0 \left| \kappa_1 \right| e^{i\varphi_\kappa} \left(E_{m-1} + E_{m+1} \right) - \tfrac{1}{2} i\omega_0 E_m \left| \Delta\alpha \right| e^{i\varphi_{\Delta\alpha}} - \omega_0 \Omega \gamma_1 \left(E_{m+1} - E_{m-1} \right) \tag{6}$$

The frequency shift term due to the self-coupling coefficient $\Delta\alpha$ can be eliminated from (6) by substituting $E_m(t) = \tilde{E}_m(t) \exp\left(-\tfrac{1}{2} i\omega_0 \Delta\alpha \cdot t \right)$. Similarly, the imaginary part of $\Delta\alpha$ can be absorbed into the photon lifetime. Next, we introduce the cavity photon lifetime and the gain into (6), as well as, the rate equation for the carrier population inversion:

$$\begin{aligned}
\frac{d\tilde{E}_m}{dt} &= \tfrac{1}{2} \left[G\left(N_m \right) - \tau_p^{-1} \right] \left(1 + iR \right) \tilde{E}_m + \tfrac{1}{2} i\omega_0 \kappa_1 e^{i\varphi_\lambda} \left(\tilde{E}_{m-1} + \tilde{E}_{m+1} \right) - \omega_0 \Omega \gamma_1 \left(\tilde{E}_{m+1} - \tilde{E}_{m-1} \right) \\
\frac{dN_m}{dt} &= P - N_m \tau_s^{-1} - G\left(N_m \right) \left| \tilde{E}_m \right|^2
\end{aligned} \tag{7}$$

where N_m is the excess carriers in laser m, P is the pump level, τ_p and τ_s are correspondingly the photons and carriers lifetimes and R is the linewidth enhancement factor connecting the change in the gain level of the semiconductor material with the change in it refractive index. $G(N_m)$ is the optical gain in laser m given by: $G\left(N_m \right) = G\left(N_{th} \right) + g \cdot \left(N_m - N_{th} \right)$ where γ is the differential gain $\partial G / \partial N$ at threshold and $G(N_{th}) = 1/\tau_p$. Finally, we normalize the rate equations according to the conventions of Ref. 8: $A_m = \sqrt{\tfrac{1}{2} g \tau_s} E_m, Z_m = \tfrac{1}{2} N_{th} g \tau_p \left(N_m / N_{th} - 1 \right)$, $p_m = \tfrac{1}{2} N_{th} g \tau_p \left(P_m / P_{th} - 1 \right)$ where $P_{th} = N_{th} / \tau_s$, $\eta = \tfrac{1}{2} \omega_0 \tau_p \left| \kappa_1 \right|$, $\eta_1 = \omega_0 \tau_p \left| \gamma_1 \right|$, $T = \tau_s / \tau_p$, $\tau = t / \tau_p$. Introducing the normalized variables to (7) yields the following normalized rate equations:

$$\dot{A}_m = Z_m\left(1+iR\right)A_m + i\eta e^{i\varphi_\eta}\left(A_{m+1}+A_{m-1}\right) - \eta_1\Omega\left(A_{m+1}-A_{m-1}\right)$$
$$T\cdot\dot{Z}_m = p_m - Z_m - \left(1+2Z_m\right)\left|A_m\right|^2 \qquad (8)$$

where the dot indicates a derivative with respect to τ. For a circular array consisting of L lasers the boundary conditions are $A_0=A_L$ and $A_{L+1}=A_1$. Eq. (8) possesses the functional form of the conventional rate equations but with an additional term which is linearly dependent on the mechanical rotation rate, Ω, and a new coupling coefficient, η_1, defined by the overlap integral in (5).

3. THE LASING MODES IN THE ROTATING FRAMEWORK

To study the dynamics and lasing properties of the circular arrays subjected to mechanical rotation, Eq. (8) were solved numerically using a fourth order Runge-Kutta integration scheme[7]. For simplicity it was initially assumed that the two coupling coefficients between adjacent micro-lasers (η and η_1) and the pumping levels (p_m) are identical for all the lasers in the array. An array consisting of L lasers has L eigen-modes of which L-1 (L-2) are degenerate for an odd (even) L. The degenerate modes correspond to CW and CCW rotating waves. The non-degenerate modes of the array are the in-phase (no phase shift between adjacent lasers) and the anti-phase (π phase shift between adjacent lasers) modes which are stationary (standing waves). In should be noted that, in a circular array of odd L the anti-phase mode does not exist due to phase frustration[9] and, therefore, for such arrays there is only a single non-degenerate eigen-mode.

For rotation sensing applications we are interested in the beating frequency generated due to the rotation induced splitting of originally degenerate CW and CCW rotating modes. Therefore, the non-degenerate solutions are unusable (see e.g. Refs. 9 and 10 for a general discussion on the role of mode-degeneracy under rotation). However, it is well known that (non-degenerate) anti-phase mode tends to be the dominant lasing solution in coupled laser arrays, having the lowest lasing threshold[12]. On the other hand, the in-phase mode generally has the highest threshold level and is seldom exhibited unless specific arrangements are made[12]. Therefore, in order to suppress the anti-phase lasing mode, it is advantageous to use an array of odd number of lasers.

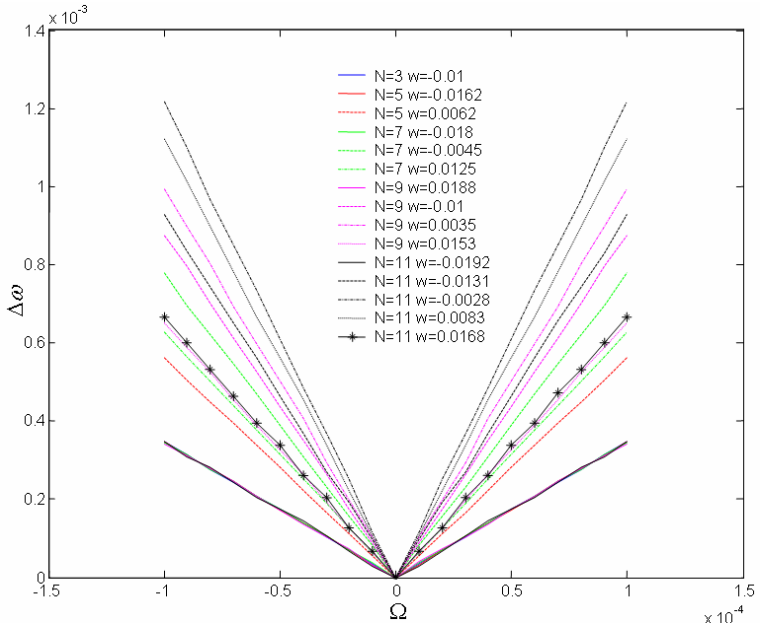

Fig. 2. Beating frequency of the different modes of CROW Gyro with 3-11 cavities. R=0, p=0.1 and T=300. The parameter w indicates the shift of the specific resonance frequency of each CROW mode from the resonance of the individual cavity in normalized frequency $w = (\omega-\omega_0)\cdot\tau/2\pi$

Figure 2 depicts the (normalized) beating frequency as a function of the (normalized) rotation rate for the various lasing modes of circular arrays consisting of 3-11 micro-lasers. The coupling coefficient η=0.01 is identical for all the arrays and $-10^{-4} < \eta_1\Omega < 10^{-4}$. The rest of the parameters are defined in the figure caption. Each curve in the figure corresponds

to the rotation induced frequency difference of originally degenerate CW and CCW rotating waves, and is designated by the (normalized) frequency shift of the degenerate modes (i.e., at Ω=0) from the resonance frequency of the individual cavity.

Figure 2 illustrates several important properties of the active CROW rotation sensor. The responsivity of Gyro, represented by the slope of the curves, is mode dependent, i.e. each (originally) degenerate mode exhibits different splitting when subjected to rotation. As can be expected, the mode with highest sensitivity is the one for which the resonance frequency is closest to that of the individual laser. This is because the slope of the dispersion relation is steepest at this point. Another prominent characteristic is the increase in the responsivity for larger array. This trend is not surprising as it stems directly from the corresponding increase in the device area (assuming the inter-laser distance remains constant).

4. STRUCTURE VARIATIONS – THE FORMATION OF A DEAD-ZONE

In ideal structures, such as the ones analyzed in section 3, the resonance wavelengths and inter-laser coupling are identical. In real-world devices, fabrication errors and tolerances induce random variations of these parameters around some mean values.

We start our analysis by noting that under stationary conditions (Ω = 0), the *entire* structure possesses second order mode degeneracy at each of its optical resonances; it supports two modes propagating in CW and CCW directions. Alternatively, since any linear combination of degenerate modes is by itself a degenerate mode, these modes can be equally well presented as two *real* standing waves. When the structure rotates, the corresponding degenerate resonance splits into two distinct resonances[9]. Similarly, structural disorder splits mode degeneracy[10]. Thus, one can invoke the theory of mode-degeneracy under rotation[9] , and extend it to hold also under structure inaccuracy using essentially the tools of Ref. 10. This combined approach has three important advantages. First, it enables one to obtain quickly the general expression for the effect of rotation *and* structure inaccuracy on the mode splitting, where the fact that each global mode can be expressed as a summation of the form of tight binding theory (3) is done at a later stage, and is used only to get more explicit final results pertaining to the gyroscope dead-zone. Second, it enables one to express the structure variation using its most fundamental form – the variation of ε, while its manifestation as variation of the individual cavity resonances and its effect on the gyro dead-zone "pops out" later as derived results. Finally, this approach also reveals an interesting physical picture of two competing effects: both, structure inaccuracy and mechanical rotation break the mode degeneracy and cause resonance splitting[9, 10]. Splitting due to the former is Ω-independent, while splitting due to the latter scales linearly with Ω. The device can be used as a gyroscope only when the splitting due to rotation exceeds the splitting due to structure inaccuracy. Hence, a dead-zone in Ω is formed. This novel physical effect of competing processes is derived analytically and backed up by numerical simulations.

4.1 Theoretical analysis

Let H_Ω be the magnetic field of the entire structure, under rotation and structure variation. It satisfies the following wave equation.

$$\Theta H_\Omega = k^2 H_\Omega + ik\mathbf{L}_\Omega H_\Omega, \quad \Theta \equiv \nabla\times\left[1/\varepsilon(\vec{r})\right]\nabla\times, \quad k = \omega/c \tag{9}$$

where $\varepsilon(r)$ describes the entire dielectric structure, including structural disorder. L_Ω is the rotation operator:

$$\mathbf{L}_\Omega H_\Omega = \nabla\times\left[\boldsymbol{\beta}/\varepsilon(\vec{r})\times H_\Omega\right] + \boldsymbol{\beta}/\varepsilon(\vec{r})\times\left[\nabla\times H_\Omega\right], \quad \boldsymbol{\beta} = c^{-1}\Omega\hat{z}\times\vec{r} \tag{10}$$

At rest, and in the absence of structural disorder, the two degenerate modes $H_0^{(m)}(\vec{r})\ (m=1,2)$ of the *entire* structure satisfy:

$$\Theta_0 H_0^{(m)} = k_U^2 H_0^{(m)}, \quad \Theta_0 \equiv \nabla\times\left[1/\varepsilon_U(\vec{r})\right]\nabla\times, \quad k_U = \omega_U/c \tag{11}$$

where $\varepsilon_U(\vec{r})$ describes the entire *unperturbed* structure and ω_0 is the corresponding resonance frequency. As will be shown, rotation and structural disorder cause it to split into two different resonances. Note that $H_0^{(m)}(\vec{r})$ can always be presented as real and orthogonal set. Therefore, we have:

$$\Theta = \Theta_0 + \delta\Theta, \quad \delta\Theta = \nabla \times \left(\delta\left[1/\varepsilon(\vec{r})\right] \right) \nabla \times, \quad \delta\left[1/\varepsilon(\vec{r})\right] = \varepsilon^{-1}(\vec{r}) - \varepsilon_U^{-1}(\vec{r}) \tag{12}$$

so the wave equation (9) can be written as:

$$\Theta_0 H_\Omega - k^2 H_\Omega = (ik\mathbf{L}_\Omega - \delta\Theta) H_\Omega. \tag{13}$$

Clearly, the LHS of (13) is nothing but the conventional wave equation governing the field in the stationary and unperturbed structure. The RHS describes two effects; that of rotation and that of structural disorder. We follow now a similar analysis to Ref. 9 with the only exception that an additional term (structural disorder) appears in the RHS. The total field is a summation over $H_0^{(n)}(\vec{r})$ serving merely as building blocks:

$$H_\Omega = \sum_{n=1}^{2} a_n H_0^{(n)} \tag{14}$$

We substitute this expansion into (13), use (11), perform inner product of the resulting equation with $H_0^{(m)}$ and use their mutual orthogonality. The result is the following 2X2 matrix-eigenvalue equation for the expansion coefficients α_n and frequency splitting k-k_U

$$\begin{bmatrix} D_{11} & D_{12} \\ D_{21} & D_{22} \end{bmatrix} \begin{bmatrix} a_1 \\ a_2 \end{bmatrix} = \left(k - k_U\right) 2k_U \begin{bmatrix} a_1 \\ a_2 \end{bmatrix} \tag{15}$$

where

$$D_{mn} = -ik_U (\mathbf{L}_\Omega H_0^{(n)}, H_0^{(m)}) + (\delta\Theta H_0^{(n)}, H_0^{(m)}) = k_U^2 \Omega B_{mn} + d_{mn} \tag{16}$$

and where (f, g) is the L_2 inner-product. Clearly, the two different eigenvalues of the equation above represent the frequency splitting. The coefficients B_{nm} here were studied in detail in Ref. [9]. They depend only on the perfect (unperturbed) structure and form a skew-symmetric imaginary matrix, with B_{11}=B_{22}=0. d_{mn} depend only on δΘ and therefore represent only structure disorder effects. By careful examination one can show that d_{12}=d_{21} and d_{11}+d_{12}→0 as the number of (statistically independent) micro-cavities comprising the entire structure, increases. Thus, we are left with the following analytical expression for the frequency splitting:

$$k - k_U = \pm \frac{1}{2k_U} \sqrt{d_{12}^2 - d_{11} d_{22} + k_U^4 \Omega^2 \left|B_{12}\right|^2}. \tag{17}$$

Thus, the splitting *vs.* Ω clearly possesses the form of Hyperbola, with a "dead-zone" Ω_d originating from the "competition" between disorder-induced splitting and rotation-induced splitting. It is given by:

$$\Omega_d \approx \left(d_{12}^2 - d_{11} d_{22}\right)^{1/2} \Big/ \left(k_U^2 \left|B_{12}\right|\right) \tag{18}$$

as shown in Fig. 4. It can be shown analytically that the d_{mn} coefficients, responsible for the dead-zone extent, are directly related to the variance of the individual cavity resonance frequency[10, 13].

4.2 Numerical results

A numerical statistical analysis of the impact of fabrication errors was performed for a 7-cavity circular CROW. The coupling coefficient between adjacent cavities was set to be $\eta = 0.01$ and the normalized rotation rate is scanned between $-10^{-4} < \eta_1\Omega < 10^{-4}$. For an ideal structure (all cavities having identical resonance frequency) the stationary system has 4 resonance frequencies where three of them are doubly degenerate. Under rotation the degeneracy is lifted and a beat signal between the originally degenerate modes is formed. Fig. 3 shows the frequency of the beat signal of an ideal system undergoing rotation. The three lines correspond to the three different degenerate modes.

xxx

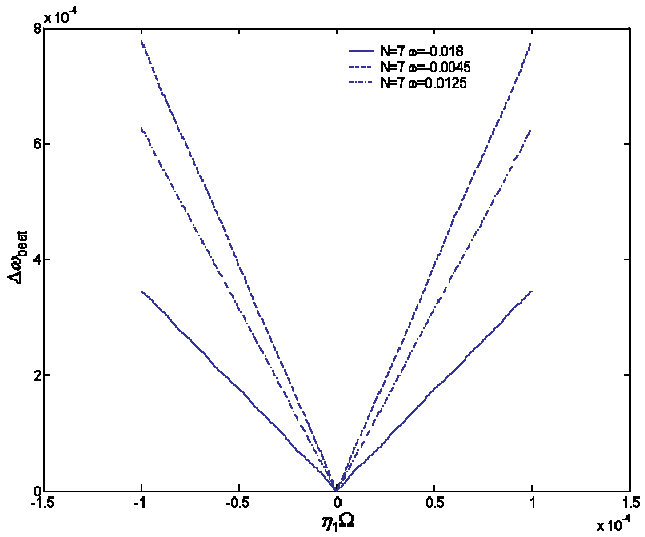

Fig. 3. Beating frequencies of an ideal rotating CROW consisting of seven cavities. The parameters are as in Fig. 2.

Fabrication errors are modeled by introducing shifts (deviations) in the resonance frequencies of the individual cavities. The deviations lift the degeneracy of the modes and, as a result, there is a beat frequency even without rotation. More over, at low rotation rates the sensitivity of the Gyro is reduced. The differences between the resonance frequencies of the cavities comprising the CROW are assumed to be normally distributed with variance σ. Fig. 4 shows the frequency of the beat signal of a "realistic" CROW Gyro with $\sigma = 10^{-3}$.

The stars indicate the numerically calculate beat frequency while the solid line represent a fit to hyperbola - $\Delta\omega_{\text{beat}} = \sqrt{a^2 + b^2(\eta_1\Omega)^2}$. Fig. 4 illustrates the decrease of the Gyro sensitivity for lower rotation rates. The excellent agreement of the numerical data to the hyperbolic fit (as predicted by the analysis of section 4.1) enables the extraction of the sensitivity (the slope of the linear parts of the hyperbola) and the "dead-zone" – the minimal rotation rate that can be detected by the Gyro.

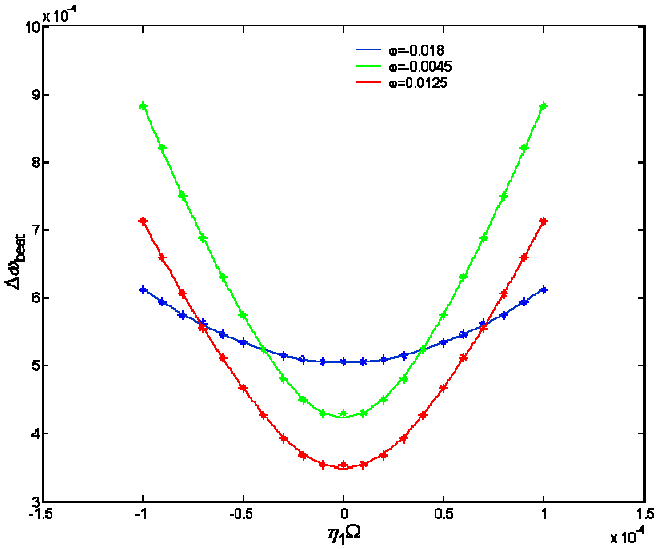

Fig. 4. Beating frequencies of a realistic rotating CROW consisting of seven cavities. The parameters are as in Fig. 2, the standard deviation of resonance of the individual cavities is $\sigma = 10^{-3}$..

An intuitive method to define the sensitivity is to calculate at the slope of hyperbola:

$$\frac{d\omega_{\text{beat}}}{d(\eta_1\Omega)} = \frac{b}{\sqrt{1+(a/b)^2\cdot(\eta_1\Omega)^{-2}}} \tag{19}$$

For large rotation rate the slope is almost constant but when $\eta_1\Omega$ becomes smaller than a/b the slope starts to decrease. Therefore, it is reasonable to define the minimal detectable (normalized) rotation rate as $(\eta_1\Omega)_{\min} = a/b$, where a and b are the hyperbola parameters found from the fit.

The statistical analysis was performed by evaluating the sensitivity and dead-zone for σ ranging between 10^{-3} and $5\text{x}10^{-3}$ (in the normalized time units). For each σ, 10 different structures where analyzed and the average slope and $(\eta_1\Omega)_{\min}$ were found for each of the three beat signals. Fig. 5 depicts the average dead-zone (a) and the sensitivity (b) for different σ.

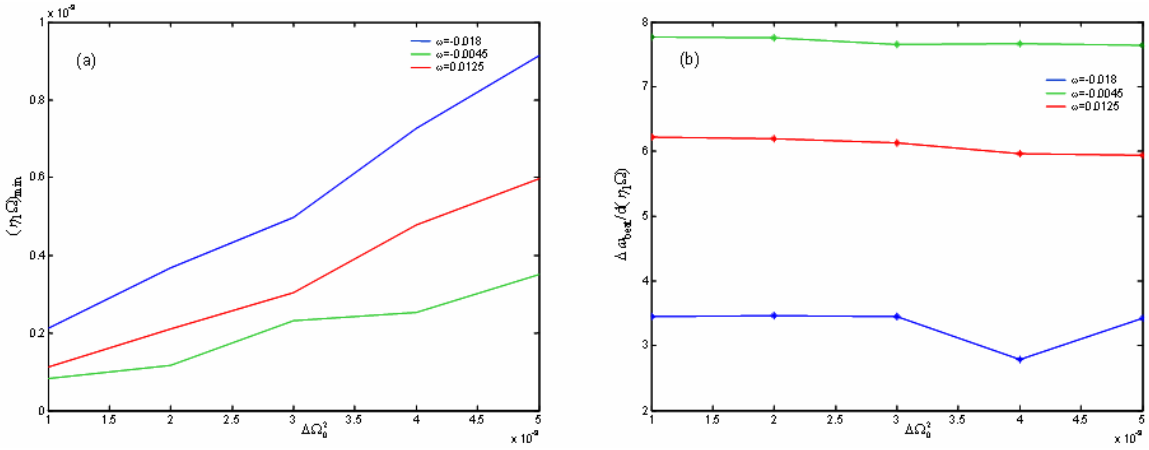

Fig. 5. Dead-zone (a) and sensitivity (b) of a "realistic" CROW as a function of σ. The rest of the parameters are as in Fig. 2

Two points that are clearly indicated in Fig. 5 The sensitivity is relatively independent of the fabrication errors – only a minor decrease of the slope is observed when the resonance frequency variance is increased. The dead-zone, on the other hand, increases significantly as σ is increased. Similar increase in the dead-zone is found for the three different modes.

5. DISCUSSION AND SUMMARY

Closed loop slow light structures based on coupled micro cavities form a novel approach for the realization of ultra-compact, chip level, rotation sensors. The incorporation of optically active cavities (i.e. lasers) can counteract the impact of optical loss (existing in passive structures) which is the main factor limiting the achievable sensitivity in CROW rotation sensors. We studied the dynamical behavior of closed-loop coupled laser arrays under mechanical rotation with applications to sensing. We found that fabrication tolerances generate a "dead-zone", similar to that found in conventional laser gyros, which depends on the variations of the individual lasers. This dead-zone is formed because the originally degenerate modes of the circular arrays split in the presence of fabrication errors. This splitting limits the minimal rotation rate that can be detected by the gyro (the rotation induced frequency different must exceed the original splitting). Although the underlying mechanism of the dead-zones observed conventional laser gyros is different (back scattering), the physics is similar. In both cases the ideal degeneracy between the CW and CCW propagating modes is removed and the Sagnac effect must exceed the frequency splitting in order to be observed.

However, we expect that as we increase the number of laser composing the gyro *while keeping structural disorder at a constant level*, the dead-zone will decrease and the minimal detected rotation rate will be reduced. This is in contrast to conventional gyros in which the length of the loop does not affect the dead-zone.

REFERENCES

[1] S. Ezekiel in *Optical Fiber Rotation Sensing*, edited by W. K. Burns, Academic Press Inc., Boston, 1994.

[2] H. J. Arditty and H. C. Lefevre, "Sagnac Effect in Fiber Gyroscopes," **Opt. Lett. 6**, 401-403 (1981).

[3] B. Z. Steinberg, "Rotating photonic crystals: A medium for compact optical gyroscopes," **Phys. Rev. E 71**, 056621 (2005).

[4] J. Scheuer and A. Yariv, "Sagnac effect in coupled resonator slow light waveguide structures,'' **Phys. Rev. Lett. 96**, 053901 (2006).

[5] B. Z. Steinberg, J. Scheuer and A. Boag, "Rotation-induced superstructure in slow-light waveguides with mode-degeneracy: optical gyroscopes with exponential sensitivity", **J. Opt. Soc. Am. B. 24**, 1216 (2007).

[6] J. Scheuer, G. T. Paloczi, J. K. S. Poon and A. Yariv, "Coupled Resonator Optical Waveguides: Towards Slowing and Storing of Light", **Opt. Photon. News 16**, 36 (2005).

[7] J. Scheuer, "Slow propagation of externally injected light pulses in coupled semiconductor laser array," **Europhysics. Lett.** 77, 44004 (2007).

[8] S. S. Wang, and H. G. Winful, "Dynamics of phase-locked semiconductor laser arrays", **App. Phys. Lett. 52**, 1774-1776 (1986).

[9] B. Z. Steinberg and A. Boag, "Splitting of microcavity degenerate modes in rotating photonic crystals – the miniature optical gyroscopes," **J. Opt. Soc. Am. B 24(1)**, 142 (2007).

[10] B. Z. Steinberg, A.Boag, and R. Listitsin, "Sensitivity analysis of narrowband photonic crystal filters and waveguides to structure variationas and inaccuracy," **J. Opt. Soc. Am. A. 20(1)**, 138 (2003).

[11] T. Fishman T and M. Orenstein, "Cyclic vertical cavity semiconductor laser arrays with odd numbers of elements: Lasing modes and symmetry breaking," **Opt. Lett. 21(8)**, 600-602 (1996).

[12] H.-J. Yoo, J.R. Hayes, E.G. Paek, A. Scherer and Y.-S. Kwon, "Array mode analysis of two-dimension phased arrays of vertical cavity surface emitting lasers," **IEEE J. Quantum Electron. 26**, 1039-51 (1990).

[13] J. Scheuer and B. Z. Steinberg, "Passive and active Slow-Light rotation sensor," in preparation